Hikaru Tamura,<sup>1,\*</sup> Cheng-An Chen,<sup>1,†</sup> and Chen-Lung Hung<sup>1,2,‡</sup>

<sup>1</sup>Department of Physics and Astronomy, Purdue University, West Lafayette, IN 47907, USA <sup>2</sup>Purdue Quantum Science and Engineering Institute, Purdue University, West Lafayette, IN 47907, USA (Dated: August 9, 2023)

Unveiling non-equilibrium dynamics of solitonic and topological defect structures in a multidimensional nonlinear medium is a current frontier across diverse fields. One of the quintessential objects is a ring dark soliton (RDS), whose dynamics are expected to display remarkable interplay between symmetry and self-patterned topological defect formation from a transverse (snake) instability but has thus far evaded full experimental observations. Here, we report an experimental realization of RDS generation in a two-dimensional atomic superfluid trapped in a circular box. By quenching the confining box potential, we observe an RDS emitted from the edge and its peculiar signature in the radial motion. As an RDS evolves, we observe transverse modulations at discrete azimuthal angles, which clearly result in a patterned formation of a circular vortex dipole array. Through collisions of the vortex dipoles with the box trap, we observe vortex unbinding, vortex pinning to the edge, and emission of rarefaction pulses. Our box-quench protocol opens a new way to study multidimensional dark solitons, structured formation of topological defects, and potentially the dynamics of ordered quantum vortex matter.

Vortices and dark solitons are fundamental defect 39 pairs. This fascinating process, called transverse instabilics and microscopic characters of the hosting medium. A quantized vortex emerges as a result of a topologically protected singularity with a  $2\pi$  phase winding. In uantum gases, beginning with seminal experiments with dynamical optical imprinting techniques [1], vortices are also produced by injecting angular momentum through stirring [2–7]. Several other techniques have been discovered [8]. While most experiments have excited disordered vortices with equal or both circulations or a vortex lattice of the same charges [2, 3], few-vortex structures with engineered flow patterns were realized only recently [9, 10]. A dark soliton, on the other hand, features a phase jump across a non-topological defect in the wave function, and is discovered primarily through phase [11– 13], density [14, 15], or state [16, 17] engineering techniques or by matter-wave interference [18–20]. By driving a quantum gas through a continuous phase transition, both vortices and solitonic defects are found to form spontaneously via the Kibble-Zurek mechanism [21–25], indicating their complimentary roles in a universal defect formation process.

Remarkably, in two or three dimensions, dark solitons are fundamentally connected to highly ordered vortex states of complex phase patterns through an intrinsic instability [26], where a self-amplifying transverse modulation can fragment a stripe (or plane) of phase defect into an ordered array of vortex and antivortex (line/ring)

2

5

6

9 structures that appear in nonlinear physics at all scales, 40 ity (TI), has been under heavy investigations in diverse from superfluids, nonlinear optics, to the cosmic fluid. 41 fields for decades [27], including also quantum gas exper-They play critical roles in understanding the dynam- 42 iments [13, 14, 16, 19, 28, 29]. In previous experimental 43 studies, however, vortices were often observed as disor-44 dered decay products of dark solitons. Self-patterned, 45 ordered vortex dipole arrays have never been clearly vi-46 sualized.

> Controlling soliton generations and its instability could 48 open a doorway towards forming complex vortex struc-49 tures that are arduous to be artificially reached. In a two-50 dimensional (2D) quantum fluid, an interesting example 51 emerges from a ring dark soliton (RDS) [30] that man-52 ifests as a circular dark stripe formed under rotational 53 symmetry. An RDS does not disperse due to the balance 54 between self-defocusing and wave dispersion [31, 32], sim-55 ilarly to straight counterparts, and naturally exhibits ra-56 dial oscillations while varying its profile. Breaking rota-57 tional symmetry of an RDS feeds TI [27, 33]. This results 58 in elusive formation of a vortex dipole 'necklace', which 59 consists of a circular array of vortex-antivortex pairs [34]. Remarkably, such ordered vortices with alternat-61 ing charges may exhibit a variety of many-body dynam-62 ics, including persistent revivals of structures [19, 33, 35] 63 and clusterization [35–38], which do not occur in disor-64 dered vortex matter [6, 7]. Moreover, structured vortex 65 matter can melt under significant perturbation and may eventually lead to chaos or turbulence [38–40].

> While RDS-like dark waves were previously engineered via phase imprinting in nonlinear optics [41, 42], or have 69 emerged from shock wave emissions in atomic/polaritonic 70 condensates [43, 44] and optics [45], one central question 71 concerning this study is whether self-patterned solitonic <sub>72</sub> and topological defect formation via an RDS can be con-73 trolled and clearly observed. Here, we show that a box-74 confined superfluid serves as a perfect arena [46]. RDS

<sup>\*</sup> tamurah@ims.ac.jp

<sup>†</sup> Current address: Atom Computing, Boulder, CO 80301, USA

<sup>&</sup>lt;sup>‡</sup> clhung@purdue.edu

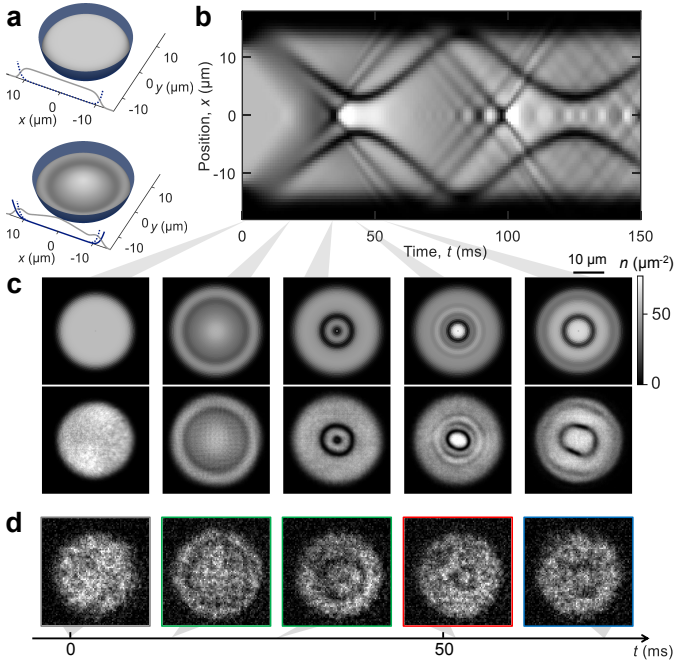
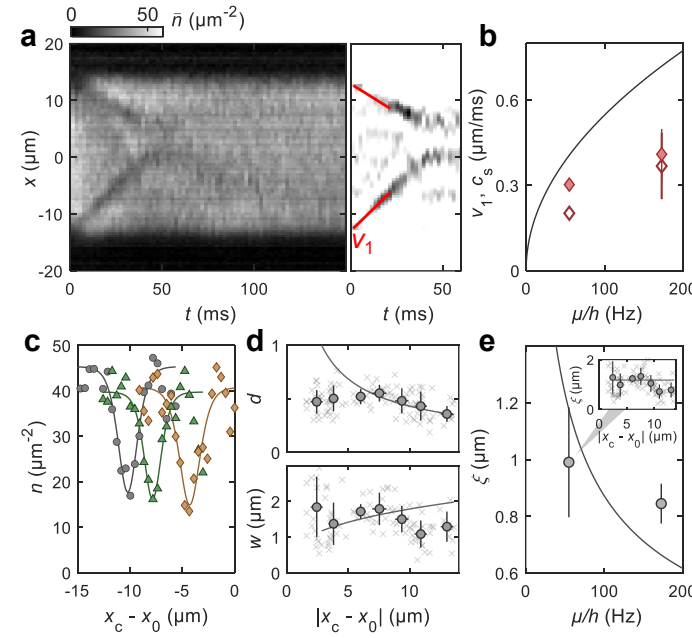


FIG. 1. Spontaneous formation of ring dark solitons. (a) A superfluid confined in a 2D circular box with a Gaussian wall (top) is subject to a potential quench-down at t=0, and emits ring dark solitons (RDSs) from the edge (bottom). (b) Time evolution of the density lineaut across the box center and (c) 2D density images (top row), evaluated using a Gross-Pitaevskii equation (GPE). Images at the bottom row are obtained at the same indicated time, but with initial density fluctuations simulated in the GPE calculation (Appendix C). Single-shot in situ images in (d) demonstrate formation of RDSs (green boxes), onset of TI (red box), and formation of vortex dipoles (blue box), respectively. Image resolution is  $\approx 0.8 \ \mu \text{m}$ .

75 formation can be realized in a box trap with a sharp wall, whose width is comparable to or smaller than the superfluid healing length. The edge profile of a superfluid can be viewed as a density defect [Fig. 1(a) top soliton described in Refs. [48, 49]. An alternative inter- 107 dynamics of quantized 2D vortex matter. pretation of this edge effect is self-interference [50], where 108 Our experimental scheme is illustrated in Fig. 1(a). an expanding superfluid bounces off the wall, and the 109 A 2D circular box is enclosed by a ring-shaped repulinterference between the bulk and the reflected flow in- 110 sive wall that has an approximate Gaussian radial produces phase slips, thus forming dark solitons. This effect 111 file  $(1/e^2)$  width  $\sim 5 \mu m$ ). The box confines a homoshould occur in quenched nonlinear systems with sharp 112 geneous 2D superfluid, with negligible thermal compoboundaries—a (D-1)-dimensional shell wave could form 113 nents, formed by cesium atoms with an initial bulk den-

from a D-dimensional system, which is difficult to be achieved with existing engineering techniques [11–20]. In this article, we report the first observation of self-  $116 \xi = 1/\sqrt{ng} \approx 1.2 \mu \text{m}$  convenient for in situ defect



Characterization of ring dark solitons. (a) Left: Time evolution of mean density linecuts  $\bar{n}(x, y_0)$ . Right: Center of the dark waves and linear fits (color lines) highlighted in a filtered image. (b) Propagation speeds of the darker waves determined at x < 0 (filled symbols) and x > 0 (open symbols), respectively. Results obtained at a higher chemical potential are plotted for comparison. Solid curve is the calculated sound speed  $v_s$ . (c) Single-shot density linecuts at t = 17.5 (circles), 23.5 (triangles), and 39.5 (diamonds) ms, respectively. Solid lines are fits. (d) Fitted depths d and widths w versus radial position from single-shots (crosses) and their means (circles). Sold lines are the case of a nonperturbed RDS, expected from Eq. (1). (e) Healing length  $\xi = w\sqrt{d}$  determined from single-shot fit results (insets). Solid lines are expectations  $\xi = \hbar / \sqrt{m\mu}$ . Error bars are standard deviations.

97 patterned defect formation in a box-confined 2D super-98 fluid. We demonstrate spontaneous RDS formation, and panel]. A quench-down of the potential height or an in- 99 unveil its radial dynamics with a symmetry-breaking teraction quench-up would effectively cause shrinkage of 100 TI at discrete azimuthal angles. We visualize structhe defect, because the edge of the superfluid expands 101 tured fragmentation of an RDS into a necklace of vortex outwards [bottom panel]. This dynamics forces the edge 102 dipoles. The observed vortex dipole structures include to emit dark solitons to conserve atom number, an effect 103 not only weakly bound vortex-antivortex pairs, but also that has recently been discussed in a case of an interac- 104 coalesced vortex cores and rarefaction pulses. They are tion quench-up with a perfect wall [47]. The mechanism 105 subject to collisions, interactions with the boundary, and is similar to an interaction quench that splits a full dark 106 annihilation, potentially showing rich non-equilibrium

117 measurements (Appendix A). The chemical potential is 171 larger chemical potential, but with the same quench pro- $_{118} \mu \approx \hbar^2/(m\xi^2) \approx k_B \times 3$  nK, where  $\hbar = h/2\pi$  is the re-  $_{172}$  tocol, are plotted for comparison. All measured veloci- $_{119}$  duced Planck constant, m is the atomic mass, and  $k_B$  is  $_{173}$  ties are significantly lower than the sound speed. We note boundary to emit a ring-shaped dark wave.

126 ics, described by a wave function that is essentially iden- 180 box, with  $(x_0, y_0) \approx (2.6, -2.2) \,\mu\text{m}$  at  $t \approx 50$  ms. For all  $\psi(r,t) = \sqrt{n} \left( i\sqrt{1-d} + \sqrt{d} \tanh \frac{r-r_c}{w} \right) e^{-i\mu t/\hbar}$ , where the dependent radius. The depth d controls that d predictions based as d predictions based as d and d predictions based as d and d predictions based as d predictions as d predictions based as d predictions based as d predictions based as d predictions as d predictions as d predictions based as d predictions as 130 the radial velocity  $\dot{r}_{\rm c}=\pm v_{\rm s}\sqrt{1-d}$  and the characteristic width  $w = \xi/\sqrt{d}$ , where  $v_s = \hbar/m\xi$  is the sound speed.  $_{\rm 132}$  Unlike linear dark solitons, the depth of an RDS does not 133 remain constant but acquires an adiabatic radial dependence to conserve its energy (Appendix B),

$$d \approx d(t_i) \left[ \frac{r_{\rm c}(t_i)}{r_{\rm c}} \right]^{2/3} ,$$
 (1)

where  $d(t_i)$  and  $r_c(t_i)$  are the initial conditions. Both 136 radial speed and width also pick up their radial depen-137 dences accordingly. For a shrinking RDS, the maxi- $_{\mbox{\tiny 138}}$  mum depth (d = 1) can be reached at a minimum ra-139 dius  $r_{
m min}=r_{
m c}(t_i) \acute{d}(t_i)^{3/2}\gtrsim \xi.$  At this point, the ra-140 dial motion would come to a complete stop, followed 141 by expansion [30]. For a shallower or smaller RDS with  $r_{\rm c}(t_i)d(t_i)^{3/2} \lesssim \xi$ , it could collapse into a single defect.

Numerical evaluation of a GPE (Appendix C) supports 144 RDS emission from this quench protocol. As shown in 145 Fig. 1(b, c), initially two distinct RDSs can be seen to 146 emerge from the edge of the wave function. A slowermoving, darker ring shrinks until it reaches the maximum 148 depth and a minimum radius. The ring then rebounds 149 and expands radially. Another shallower, faster-moving 150 ring appears to collapse at the center but would emerge again as an expanding ring. Both RDSs are later reflected off the box wall as discussed in a case of 1D solitons [51], exhibiting bouncing dynamics periodically. These boxtrapped RDSs cross each other multiple times with preserved shapes, and appear to be long-lived if rotational symmetry is not explicitly broken. They do however radiate additional shallow RDSs after collapsing at the box center, when the radial motion becomes non-adiabatic.

We experimentally confirm RDS emission from in situ 160 images of box-quenched superfluids. Figure 1(d) shows qualitative correspondences between single-shot experi-162 ment density profiles and GPE results. A prominent dark  $_{163}$  ring is clearly visible within  $t\lesssim 50$  ms until a minimum  $_{218}$  Therefore, high frequency modulations stop growing as 164 radius is reached. Linecut density [Fig. 2(a)] averaged 219 an RDS shrinks down. Around the minimum radius, only 165 over different experimental shots clearly shows the dark 220 the most unstable mode(s) with  $l=l_{\rm max}\lesssim r_{\rm min}/\xi$  could  $_{166}$  ring's radial bouncing dynamics. A less visible, shal-  $_{221}$  continue to amplify, until the RDS fragments into  $\sim l_{\rm max}$ <sub>167</sub> lower dark wave is found to cross near the box center <sub>222</sub> pieces with angular separation  $\Delta \phi \approx 2\pi/l_{\rm max}$ . at  $t \approx 30$  ms, similar to the GPE result [Fig. 1(b)].

<sub>170</sub> shown in Fig. 2(b). Wave speeds from samples with a <sub>225</sub> tion in the dark ring,  $C_{\Delta\phi} = \langle C(\phi, \Delta\phi) \rangle_{\phi}$ 

the Boltzmann constant. At time t = 0, the height of the 174 that there is an anisotropy in the observed wave velocities wall potential is quenched from  $\approx k_B \times 35 \,\mathrm{nK}$  to  $9 \,\mathrm{nK}$ . 175 across the box center. This originated from an azimuthal Due to the much reduced repulsion from the Gaussian 176 variation in the wall width, which is due to aberration in wall, the superfluid would expand outwards, forcing the 177 our optical potential, and this gives a slight anisotropy in 178 the soliton depth and radial velocity as well. As a result, One signature of an RDS is its radial collapse dynam- 179 the dark ring center appears to be drifting slightly in the tical to a 1D dark soliton in the radial coordinate [30], 181 quoted positions in the following analyses, the shift has

The observed radial dynamics can be compared with 184 predictions based on Eq. (1) and the measured initial 185 conditions. From the initial wave velocity  $(v_1 = \dot{\bar{r}}_c \approx$  $_{\rm 186}~0.3\,\mu{\rm m/ms})$  and ring radius  $\bar{r}_{\rm c}\approx 11~\mu{\rm m}$  measured at  $_{\text{\tiny 187}}$   $t_i$   $\approx$   $13\,\text{ms},$  the dark ring is expected to reach a mini- $_{\mbox{\tiny 188}}$  mum radius  $r_{\mbox{\tiny min}} \approx 3\,\mu\mbox{m},$  agreeing well with our observation  $\approx 3.2 \,\mu\text{m}$ . To compare the entire density evolution 190 with expectations, we fit the detected ring density dips [Fig. 2(c)] with  $n(x) = |\psi(x,t)|^2$ , and extract the width 192 w as well as depth d versus position of the defect cen-193 ter  $x_c$  in (d). We compare the relationship  $\xi \approx w\sqrt{d}$  in (e). The results are consistent with predictions assuming 195 a perfectly unperturbed RDS, except that the measured 196 depth stops to increase with decreasing ring size at ra-197 dius  $\lesssim 5 \ \mu \text{m}$ . We attribute this reduced contrast to an 198 instability developing in the dark ring – as we shall now 199 discuss.

An RDS becomes unstable when the rotational sym-201 metry is broken [33], which in experiment occurs in the 202 presence of thermal and quantum fluctuations or with 203 an azimuthal variation in the generating box potential. 204 An RDS would suffer transverse modulations from self-205 amplifying noise. This is clearly visible in our experi-206 ments especially when the dark ring reaches the minimum <sup>207</sup> radius, as seen in Fig. 1(d). Seeding initial fluctuations in 208 an otherwise smooth GPE wave function (Appendix C), 209 qualitatively similar density perturbations are observed 210 in Fig. 1(c).

Interestingly, TI is intrinsically coupled to an RDS's 212 radial motion. For a dark soliton stripe with finite  $_{213}$  length L, it is known that TI manifests as sinusoidal 214 'snaking' density modulations along the stripe, with dis-215 crete wavenumbers  $k_l = 2\pi l/L \lesssim 1/w \ (l \in \mathbb{N})$  limited  $_{216}$  by the transverse width w [52]. In an RDS, this sets a 217 radius-dependent limit,

$$l \lesssim \frac{r_c}{w} \sim \frac{\sqrt[3]{r_{\min} r_c^2}}{\xi}$$
 for  $l = 1, 2, 3, \dots$  (2)

To visualize this dynamics, in Fig 3(a) we Initial radial velocities of the darker  $(v_1)$  rings are  $v_2$  plot the angular density-density correlation func-

 $\langle \langle n_{\phi} n_{\phi + \Delta \phi} \rangle - \langle n_{\phi} \rangle \langle n_{\phi + \Delta \phi} \rangle \rangle_{\phi}, \text{ where } n_{\phi} = n(r_{c}, \phi)$ 227 is the atomic density near the measured ring position  $r = r_c$ , and  $\langle \cdot \rangle$  ( $\langle \cdot \rangle_{\phi}$ ) denotes ensemble (azimuthal) 229 averaging. After a long enough time while the dark ring 230 approaches its minimum radius, we observe very strong <sub>231</sub> angular correlations at  $\Delta \phi \approx 120^{\circ}$  and 240° angles, 232 corresponding to l=3. This mode appears to create 233 radial distortions of a triangular-shape, as exemplified 234 by the single-shot images in the second column of 235 Fig. 4(a). Interestingly, as the dark ring continues to 236 evolve ( $t \gtrsim 50 \, \mathrm{ms}$ ), a new correlation pattern develops at around 180° angle, that is, for  $l \leq 2$ ; see the images in the third column of Fig. 4(a).

To observe this mode competition more clearly, we 240 measure the Fourier spectrum by evaluating  $A_l$  =  $\left\langle \left| \sum_{\Delta\phi} C(\phi, \Delta\phi) e^{il\Delta\phi} \right| \right\rangle_{\phi}$ . As shown in Fig. 3(b), instability develops mostly within  $l \leq 6$ , whose amplitudes 243 are exponentially amplified as shown in (c). Figure 3(d) 244 plots the initial growth rate for each mode, quantita-245 tively reproduced by the GPE simulations detailed in Appendix F. In the experiments, the l=3 mode is the most unstable with the largest growth rate. At  $t \gtrsim 40$  ms, however, the growth of high frequency modes become arrested by the shrinking radius. The onset of growth suppression roughly follows the estimation given by Eq. (2), <sup>251</sup> until the minimum ring radius is reached; see (b). Beyond  $_{252}$   $t \gtrsim 50$  ms, l = 1 and 2 modes continue to amplify un-253 til  $t \gtrsim 70\,\mathrm{ms}$  when  $A_{l=1,2}$  become large enough to break 254 the expanding dark ring. In real space, this corresponds <sub>255</sub> to fragmentation of  $l_{\text{max}} = 2$  pieces with 180° angular 256 separation as evidenced in our observations.

We identify these self-structured fragments as vortex dipoles [34] in which the vortex-antivortex distance  $\Delta$  is linked to the speed  $v_{\rm d} \sim \hbar/m\Delta$  and the incompressible kinetic energy of the flow  $E \sim \log(\Delta/\xi)$ . Remarkably, we observed a variety of vortex dipole structures in experiment and in GPE simulations as well [Fig. 4(b)]; many of these structures were classified in Refs. [53, 54]. One type of defect is referred to as a weakly bound vortex dipole, appearing when the flow has a larger energy. It features two well-separated cores and phase singularities as shown in (i). A second type of defect is a rarefaction pulse shown in (ii), which shows a phase step without vorticities and propagates at a velocity closer to the sound speed. It emerges as a local density minimum weakly connected to other defects in the bulk or at the boundary. A third type, which we observe most frequently, is somewhat in between the first two. Its energy is large enough to preserve two phase vorticities but too small to separate their cores. It can be seen as an isolated density defect with an elongated width  $(\geq 2w)$  and is identified as a bounded dipole as in (iii). Oftentimes, the second and the third types of defects are referred to as coalesced vortices [55] or Jones-Roberts solitons [56].

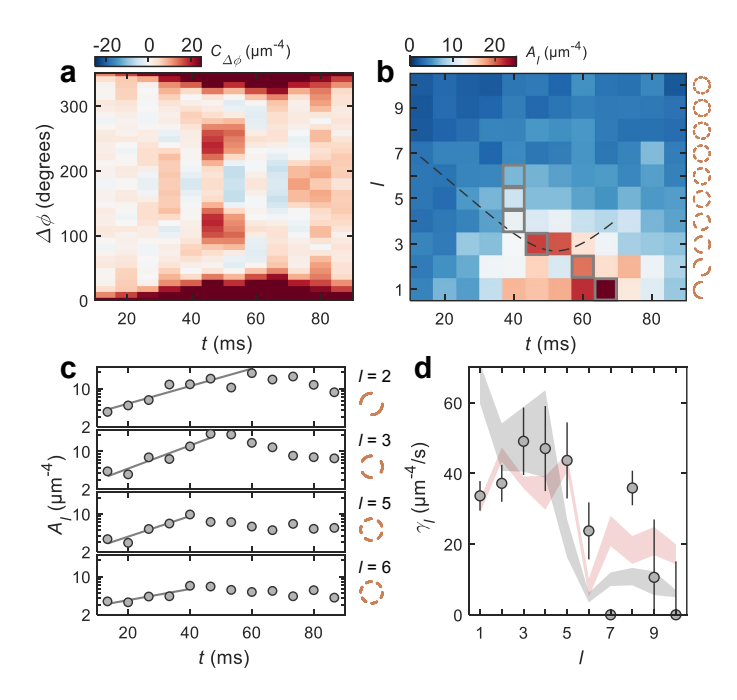


FIG. 3. Pattern-forming instability. (a) Evolution of the azimuthal density-density correlation function  $C_{\Delta\phi}$  showing pattern formation. (b) Fourier spectra  $A_l$  showing mode competition. Peak position of each mode  $(l \leq 6)$  is marked by a gray square. Dashed line marks the calculated thresholds, Eq. (2), below which modes are expected to be unstable. (c) Fourier amplitude  $A_l$  of indicated modes plotted in the logarithmic scale. Solid lines are exponential fits to determine the initial growth rates  $\gamma_l$  shown in (d). Red shaded band represents the GPE simulated rate, scaled by an overall constant  $\approx 0.17$  to match the data. Gray shaded band includes systematic effects in imaging, showing agreement with experiment without any adjustable parameters. Details can be found in Appendix F. Error bars in the data and vertical bands in the simulated rate represent fitting uncertainty.

283 efaction pulses (green ovals) that are weakly linked in a <sub>284</sub> triangular shape are often found at  $t \sim 50\,\mathrm{ms}$ . Pairs of 285 bounded vortex dipoles (blue ovals) are most frequently 286 identified immediately after an RDS fragments. Weakly 287 bound dipoles (brown ovals) sometimes appear, poten-288 tially due to stronger snaking modulations and a larger 289 flow energy to separate the cores. At longer times, many 290 isolated vortices (red circles) are found near the edge of 291 the box, presumably exhibiting similar orbital dynam-292 ics as seen in [57]. Detailed identification algorithms of <sup>293</sup> density defects can be found in Appendix D and E.

Clear distinction of vortex dipoles can be visualized 295 from their interaction with the wall potential, where the  $_{296}$  density gradient induces an inward force on both the vor-297 tex and the antivortex and this triggers the Magnus ef-298 fect. A vortex dipole would decelerate and unbind upon 299 hitting the wall as shown in (i) and (iii) of Fig. 4(b). 300 The unbound vortices appear pinned to the superfluid In Fig. 4(a), due to shot-to-shot fluctuations in atomic 301 boundary and move along the rim with opposite circudensity (see also Appendix E), observed density defects 302 lation. If instead a rarefaction pulse is incident upon 282 exhibit various shapes as discussed above. Three rar- 303 the wall, it forms an arc-like defect structure as shown

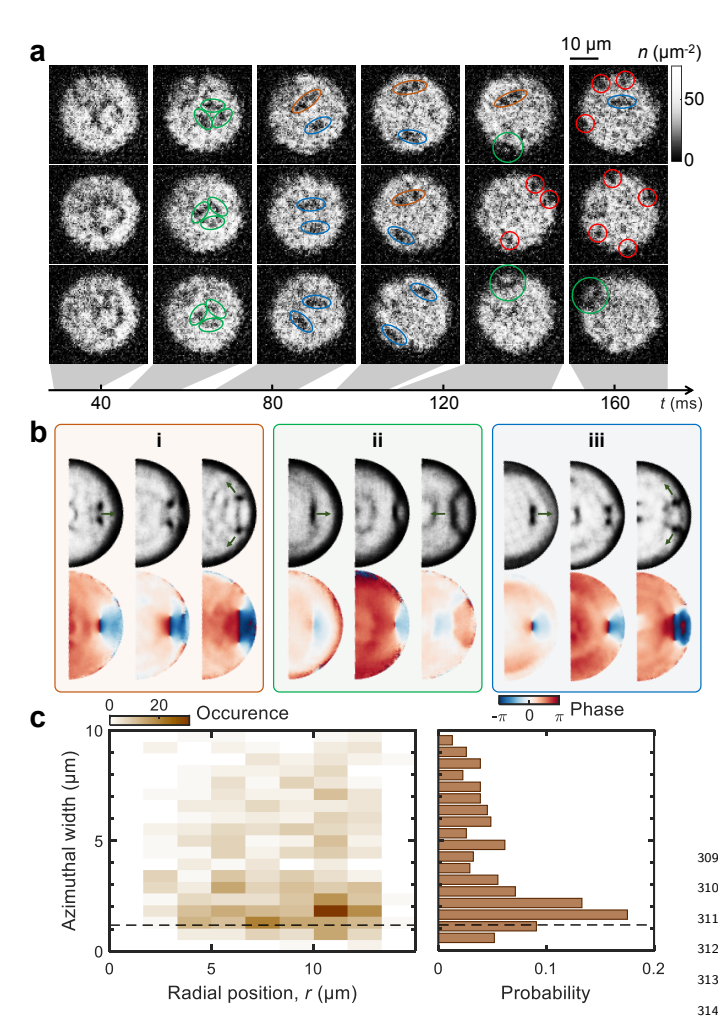


FIG. 4. Structured formation of vortex dipole necklace and vortex unbinding. (a) Single-shot in-situ images in each column are collected within the indicated time interval. The first three columns show samples right before, during, and right after patterned fragmentation, respectively. The last three columns present samples with density defects likely before, during, and after they reach the superfluid boundary. Identified density defects are circled and categorized as one of the following: weakly bound vortex dipoles (brown), rarefaction pulses (green), bounded dipoles (blue), and pinned vortices (red). (b) Dynamics of a weakly bound dipole (i), a rarefaction pulse (ii), and a bounded dipole (iii) in GPE simulations. Images in each box, from left to right, respectively, show the density (top) and phase (bottom) profiles before and after a defect hits the wall. The propagation direction of each defect is marked by an arrow. (c) Left: Occurrence of azimuthal width versus radial position of detected defects, obtained from images taken after  $t=60\,\mathrm{ms}$ . Right: Probability distribution for detected widths at  $r \geq 9 \,\mu\mathrm{m}$  showing a peak near the healing length (dashed line).

305 pulse, and occasionally also two vortices pinned to the 337 ordered ( $l_{\rm max}=3$ ) vortex dipole necklaces have been ob-306 boundary with opposite circulations. These rarefaction 338 served in Figs. 4 and 5, respectively. Even higher-order  $_{307}$  arcs are evidenced by defects marked with large green  $_{339}$   $l_{\mathrm{max}} \geq 3$  can be created with either a larger bulk chem-308 circles in Fig. 4(a). Long after all vortex dipoles have 340 ical potential (for shorter-scale most unstable modes)

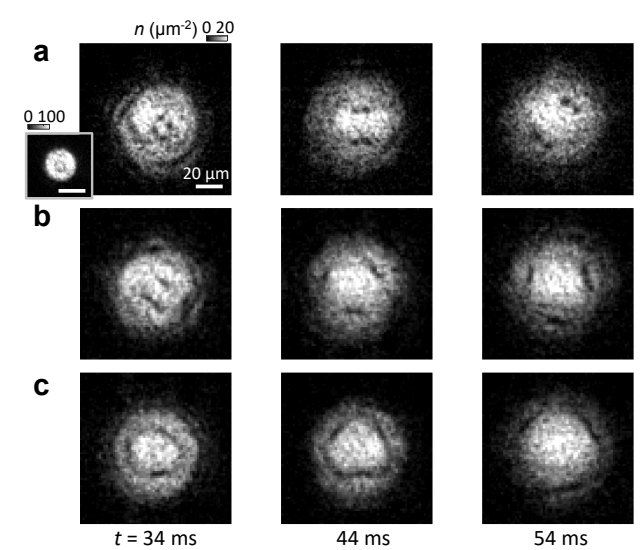


FIG. 5. Self-patterned defect structures imaged after 40 ms of time-of-flight. Single-shot images in each column are collected with the indicated hold time, showing a necklace of weakly bound vortex dipoles (a), bounded dipoles (b), and rarefaction pulses (c). Inset shows a sample in situ image at  $t = 34 \,\mathrm{ms}$ , held in a circular box of radius  $\approx 11 \,\mu\mathrm{m}$ .

309 interacted with the wall, we identified a high probabil-310 ity for observing vortex-like density defects (azimuthal  $_{311}$  size  $\sim \xi$ ) near the boundary  $r\gtrsim 9~\mu\mathrm{m}$ , as shown in  $_{312}$  Fig. 4(c). Other defects at  $r\lesssim 9~\mu\mathrm{m}$  have a wide spread  $_{313}$  of azimuthal widths ( $\gtrsim 2\xi$ ). They are likely rarefaction <sup>314</sup> pulses, rebounded dipoles, or colliding defects in the bulk.

We have demonstrated in situ images of self-structured density defects. This enables directly probing selfpatterning dynamics in a superfluid for the first time. To further enhance visualization of vortex dipole neck-319 laces, we can extinguish the horizontal trap confinement 320 and image after a long time-of-flight (TOF) expansion in 321 2D; see Fig. 5. We note that these structures continue 322 to evolve during the expansion. Here, we use a smaller 323 box to increase the initial density, chemical potential,  $_{324}$  and thus the TOF expansion rate. Vortex cores in l=2325 vortex dipole necklaces dramatically expand during TOF 326 due to much reduced healing length, clearly visible in (a). 327 As dipoles propagate towards the boundary, their core 328 size further increases due to reduced background density. We have also observed l=2 or 3 bounded dipoles (b) and <sup>330</sup> rarefaction pulses (c), identified based on their widths 331 and connections with adjacent defects. Faster moving RDSs can also be seen near the boundary of expanded 333 superfluids.

In summary, we observed very rich non-equilibrium 335 dynamics and self-patterning with RDSs that emerged  $_{304}$  in (ii), eventually breaking into a reflecting rarefaction  $_{336}$  purely from a box quench. Both  $180^{\circ}$  ( $l_{\rm max}=2$ ) and  $120^{\circ}$ 

<sub>342</sub> pendix C). Our quench experiment demonstrates a new <sub>394</sub> [67]. Typical initial density is  $n \approx 50 \, \mu \text{m}^{-2}$  at a fixed <sub>343</sub> tool to generate dark solitons in versatile forms as well <sub>395</sub> 2D interaction strength  $g = \sqrt{8\pi}a/l_z \approx 0.017$ . Shortly 344 as ordered quantum vortex matter in a uniform box trap 396 after the box potential height is quenched to the final <sub>346</sub> teraction tuning using a Fechbach resonance, multiple <sub>398</sub>  $n \approx 42 \,\mu\text{m}^{-2}$  and remains roughly constant throughout RDSs [58, 59] and vortex dipole necklaces may be gen- 399 the subsequent evolution, presumably due to initial finite <sup>348</sup> erated in one sample, thus creating complex vortex mat- <sup>400</sup> atom spilling over the box wall. The resulting healing <sub>349</sub> ter. It may be possible to trap a stationary RDS [34] <sub>401</sub> length is  $\xi = 1/\sqrt{ng} \approx 1.2 \,\mu\text{m}$ , larger than our image 350 and further control its stability by applying a radial po- 402 resolution. This allows us to resolve individual vortices  $_{351}$  tential when  $r_{\rm c}=r_{\rm min}$  [52, 60]. By incorporating non-  $_{403}$  with spacing comparable to or smaller than the healing 352 destructive imaging [61], our work can be extended to 404 length. Note that in situ imaging of vortices has been new ways to explore spontaneous clustering [62–64] in 2D 407 ing [9, 69]. vortex matter.

#### ACKNOWLEDGMENTS

We thank Eli Halperin, Qi Zhou, Samuel Alperin, 410 Chih-Chun Chien, and Sergei Khlebnikov for discussions. 411 dependent 2D Gross-Pitaevskii equation (GPE), This work is supported in part by the W. M. Keck Foundation, the NSF (Grant # PHY-1848316), and the DOE QuantISED program through the Fermilab Quantum Consortium.

### Appendix A: Preparation of a 2D superfluid

The detailed experimental apparatus is detailed in [65] with an updated objective lens (numerical aperture  $\approx 0.6$ ). We begin the preparation of a Bose-Einstein condensate (BEC) of cesium atoms confined in an optical dipole trap with horizontal (vertical) trap frequency  $_{370}$  of  $\sim 12\,\mathrm{Hz}~(\sim 70\,\mathrm{Hz})$  through an evaporative cooling pro- $_{371}$  cedure. The s-wave scattering length is then gradually decreased to a small value  $a \approx 12a_0$  via a Fechbach resonance [66], where  $a_0$  is the Bohr radius. The BEC is 374 then loaded into a 2D box potential. The vertical con-375 finement of the box is provided by a single node of a  $_{376}$  repulsive standing wave potential with  $3\,\mu\mathrm{m}$  periodic-377 ity. The measured vertical trap frequency in the node <sub>378</sub> is  $\omega_z \approx 2\pi \times 1.8 \, \text{kHz} \, (\gg k_{\rm B}T/\hbar, \, \mu/\hbar)$  deeply in the 2D regime, where  $k_B$  is the Boltzmann constant, T < 10 nK380 is the temperature,  $\mu$  is the chemical potential, and  $\hbar$  the 381 reduced Plank constant. The atoms populate the vibrational ground state in the vertical trap with a harmonic 383 oscillator length  $l_z=\sqrt{\hbar/(m\omega_z)}\approx 207\,\mathrm{nm},$  where m384 is the atomic mass. The horizontal confinement is arbitrarily configured via a blue-detuned light (780 nm) patterned with a digital mirror device and projected through the objective lens. In this work we use a circular box with <sub>388</sub> an inner radius of  $\approx 15 \,\mu\mathrm{m}$  and a width of  $\approx 5 \,\mu\mathrm{m}$ . We 389 obtain in situ density distribution of 2D gases by per-<sub>390</sub> forming absorption imaging through the same objective <sub>433</sub> where  $d(t_i)$  and  $r_c(t_i)$  are the initial depth and radius of <sub>391</sub> lens and recording the image on a CCD camera. The  $_{434}$  the RDS, determined at time  $t_i$ . This additional equa-<sub>392</sub> image resolution is  $\sim 0.8 \,\mu\text{m}$ . The atomic surface den-<sub>435</sub> tion further relates (d, w, v) with  $r_c$ . The depth increases

 $_{341}$  or larger initial short-scale density perturbations (Ap-  $_{393}$  sity n is calibrated using a similar scheme discussed in [46]. By incorporating box quenches together with in-  $_{397}$  strength ( $\approx k_B \times 9$  nK), the bulk density reduces to study inverted TI [33], persistent revivals and clusteri- 405 demonstrated using a dark-field imaging technique [68] zation [35-38] of ordered vortex dipoles, and may open 406 and most recently using high-resolution absorption imag-

# Appendix B: Wave function and radial dynamics of a ring dark soliton

An RDS is a quasi-stationary solution of the time-

$$i\hbar\frac{\partial\psi}{\partial t} = \left[ -\frac{\hbar^2}{2m} \left( \frac{\partial^2}{\partial r^2} + \frac{1}{r} \frac{\partial}{\partial r} + \frac{1}{r^2} \frac{\partial^2}{\partial \phi^2} \right) + \frac{\hbar^2 g}{m} |\psi|^2 \right] \psi . \tag{B1}$$

412 Assuming rotational symmetry, the wave function of a 413 perfect RDS only has radial dependence. To good ap-414 proximation, it can be written as

$$\psi(r,t) = \sqrt{n} \left[ i\sqrt{1-d} + \sqrt{d} \tanh(r - r_c)/w \right] e^{-i\mu t/\hbar},$$
(B2)

where  $r_{\rm c}(t)$  is the radial position of the density defect,  $d = 1 - (v/v_s)^2 \le 1$  its depth,  $v = \dot{r}_c$  its radial veloc-417 ity, and  $w = \xi/\sqrt{d}$  its characteristic width. Here, the background density n, the healing length  $\xi = 1/\sqrt{ng}$ , 419 the sound speed  $v_{\rm s}=\hbar/\xi m$ , and the chemical poten-420 tial  $\mu = mv_s^2$  are the bulk properties of the superfluid. Whereas, the radial motion v, width w and depth d are 422 all related to each other; fixing one parameter completely 423 determines the other two. A faster-(slower-)moving soli-424 ton would have a shallower (deeper) depth and a broader 425 (narrower) density profile.

This radial wave function is essentially the dark soli-427 ton solution in 1D, except that it is perturbed by the  $^{428}$   $r^{-1}\partial/\partial r$  Laplace term in the 2D GPE. A consequence of 429 this perturbation is that (d, w, v) slowly evolves as the  $_{\rm 430}$  radius of an RDS changes [30]. The dynamics of an RDS 431 differs from that of a 1D dark soliton. In particular, the 432 soliton depth follows the relation

$$d = d(t_i) \left[ \frac{r_c(t_i)}{r_c} \right]^{2/3} , \qquad (B3)$$

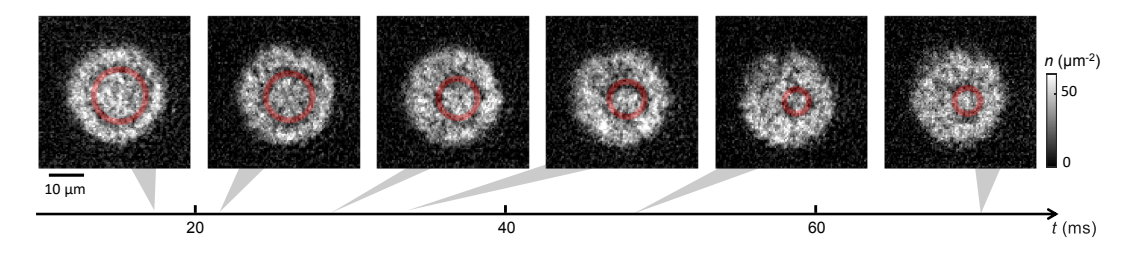


FIG. 6. Single-shot in-situ images of RDSs. The red shaded area represents the radius  $\bar{r}_c$  of produced RDSs from the averaged image. Even though RDSs fragment into multiple pieces for a longer time, their locations are efficiently captured.

and radial velocity change accordingly.

439 from energy conservation. As discussed in [70], the en-478 plus zero-point fluctuations, ergy of a 1D dark soliton is  $\epsilon = (4/3)\hbar v_s n d^{3/2}$ . For a dark soliton stripe in 2D,  $\epsilon$  is the linear energy density. In a uniform medium, the total energy of an RDS is  $2\pi r_c \epsilon$ . For an adiabatic evolution with conserved RDS total en-446 [30].

## Appendix C: Time-dependent GPE simulation

447

We perform 2D GPE simulations [71, 72] to obtain 449 numerical evidence of RDS emission in our quench protocol. The initial ground state wave function is confined 451 in a repulsive wall potential of the form

$$U(r) = \begin{cases} U_0 e^{-2(r-R)^2/\sigma^2} & r \le R \\ U_0 & r > R \end{cases}$$
 (C1)

 $_{\mbox{\tiny 452}}$  where  $U_0$  is the trap strength, R the box radius, and  $\sigma$ 453 the experimentally calibrated  $1/e^2$  width of the wall. In 454 the time-dependent GPE, the trap strength is quenched from  $U_0 = k_B \times 60$  nK to the final value  $U_f = k_B \times 9$  nK, 456 and we evaluate the subsequent dynamics of the wave 457 function. We note that in the experiment the wall has a 496 458 radial Gaussian profile of finite width instead of a semi-497 ton (RDS), we measure mean density linecuts  $\bar{n}(x, y_0)$ 459 infinite form taken in the GPE simulation. The former 498 typically averaged over > 5 realizations. By convolving 460 is responsible for finite atom spilling after the potential 499 the linecuts with a Gaussian Kernel of a width  $\sim$  the 461 is quenched down. The results shown in Fig. 1 are calcu- 500 healing length ξ, we obtain a scale-space representation 462 lated using atom number  $N=2.2\times10^4$  matching that 501 that suppresses features smaller than  $\xi$ . A Laplacian of 463 of the initial experimental condition. While we have ob- 502 this convolution generates positive features for intensity 464 tained qualitative one-to-one agreement of RDS emission 503 minima, which correspond to the mean locations of dark 465 and its subsequent evolution, the exact timing cannot be 504 stripes. These procedures are applied to the density line-466 fully matched. The emitted RDS tends to move faster 505 cuts obtained at different times t to visualize the evolu-467 in GPE simulation, and we have increased  $U_0$  by  $\sim 70\%$  506 tion of dark stripe locations, as shown in the right panel 468 to increase the quench contrast, which slows down the 507 of Fig.2(a). We then extract the stripe speed and loca-469 RDS velocity. The slower RDS dynamics observed in the 508 tion. We perform the same analysis to averaged density 470 experiment may be due to finite atom-spilling right after 509 linecuts along the y axis,  $\bar{n}(x_0, y)$ . With those informa-471 the quench, which leads to a lower sound speed and thus 510 tion obtained from the mean linecuts along the two axes, 472 a lower RDS velocity.

474 fluid, we imprint phase noise in the initial GPE wave 513 For the analysis of instability in RDSs [see Fig.3] we use

(decreases) as an RDS shrinks (expands), and the width 475 function to simulate phonon excitations. Given an initial 476 temperature  $(T \approx 3 - 7 \text{ nK})$ , we calculate the phonon An explanation for this radius-dependent dynamics is 477 populations according to the Bose-Einstein distribution

$$n_p(k) = \frac{1}{e^{E(k)/k_B T} - 1} + \frac{1}{2} = \frac{1}{2} \coth \frac{E(k)}{2k_B T},$$
 (C2)

ergy, one must have  $r_c(t_i)d(t_i)^{3/2} = r_c d^{3/2}$ , thus leading where E(k) is the Bogoliubov phonon dispersion relation. 445 to the same result obtained from the perturbation theory 480 We populate random Bogoliubov phonon excitations in 481 the ground state wavefunction, with statistical amplitude 482 variance in each mode matching  $n_n(k)$ . We then evolve 483 the wave function in the time-dependent GPE. We have 484 also taken into account total atom number fluctuations 485 in the experiment, and performed a series of GPE calculations with  $N=(2.2\pm0.4)\times10^4$ . Given the range of temperature and atom number fluctuations, we observe numerically RDS fragmentation into necklaces of 489 weakly bound vortex dipoles, tightly bound dipoles, or 490 rarefaction pulses. Representative results are plotted in 491 Fig. 4(b). Most of the necklaces consist of a chain of (C1)  $_{492}$  l=2 vortex dipoles or rarefaction pulses. Increasing the 493 atom number or interaction strength  $g, l \geq 3$  necklaces 494 can be observed.

### Appendix D: Soliton detection algorithm

To obtain the position and size of a ring dark soli-<sub>511</sub> we predict the time-dependent center  $r_0$  and radius  $r_c$ To take into account density fluctuations in a super- 512 of RDSs in single-shot images, see red areas in Fig. 6.

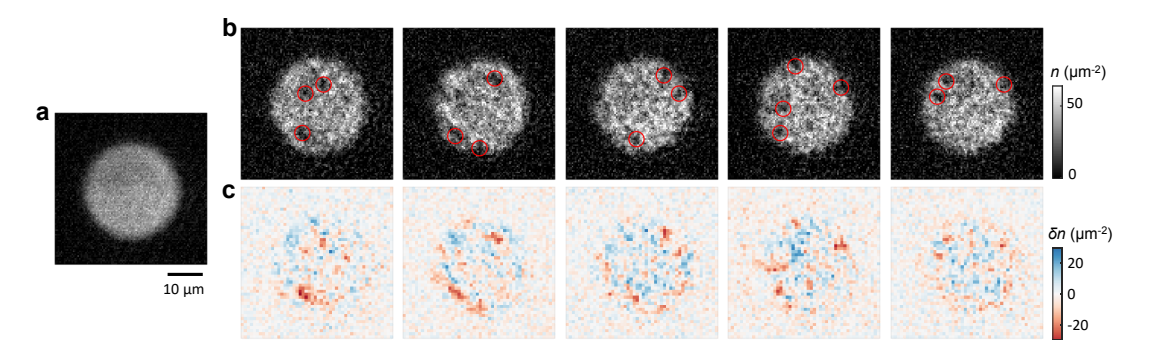


FIG. 7. In-situ vortex detection in a box-trapped 2D superfluid. (a) Mean density profile  $\bar{n}$  averaged over > 300 experimental realizations at  $> 60 \,\mathrm{ms}$ . (b) Examples of single-shot in-situ density images n. Detected defects are marked by red circles. (c) Residual from the mean density,  $\delta n = n - \bar{n}$ .

single-shot density profiles averaged in the radial interval 549 However, at a later time when  $\bar{r}_c$  approaches to its min- $|r - r_c| \lesssim 0.9 \,\mu\text{m}$ .

#### Appendix E: Vortex detection algorithm

 $^{517}$  . At later times (  $t\gtrsim60\,\rm ms)$  after the box quench, an  $^{518}$  RDS breaks into vortices. They are detected using a [73]. For each single-shot in situ image [Fig. 7(b)], we calculate the residual [Fig. 7(c)] from the mean density profile [Fig. 7(a)] averaged over many experimental shots. We then apply a Laplacian of Gaussian filter to enhance those defect structures having characteristic length scales  $_{525}$  of  $\sim \xi$ . From these we obtain defect positions marked by 526 circles in Fig. 6(b). We note that the analysis is restricted <sub>527</sub> to defects having nearly zero local density ( $\lesssim 4 \,\mu\text{m}^{-2}$ ) 528 to avoid spurious detections. Detected defects have a 529 large variation in the azimuthal width, while the radial spread is comparable with  $\sim \xi$ . The azimuthal width and position of each detected defect are analyzed as shown in  $_{532}$  Fig.4(c).

## Appendix F: Pattern formation dynamics in GPE simulation

A series of GPE simulations with initially seeded random fluctuations are analyzed according to the presented 537 data in Fig. 3 for further understanding the pattern for-538 mation by snaking instability in RDSs. We first deter- $\bar{r}_c$  of generated RDSs and its mo-540 tion  $\dot{\bar{r}}_c$  from an radial density profile [Fig. 8(a)], averaged 541 over multiple runs. We then analyze the angular density- $_{\mbox{\tiny 542}}$  density correlation function  $C_{\Delta\phi} = \langle C(\phi,\,\Delta\phi) \rangle_{\phi} =$  $_{543}$   $\langle\langle n_{\phi}n_{\phi+\Delta\phi}\rangle - \langle n_{\phi}\rangle\langle n_{\phi+\Delta\phi}\rangle\rangle_{\phi}$ , where  $\langle\cdot\rangle$   $(\langle\cdot\rangle_{\phi})$  repre-  $_{584}$  observed in the experiment is due to the systematic effect 544 sents sample (azimuthal) average and  $n_{\phi}$  is the azimuthal 585 of finite resolution of our imaging system and image noise 545 density at  $r = \bar{r}_c$ . As shown in Fig. 8(b), the simulated 586 for example, photon shot-noise, which adds to each mea-<sub>546</sub>  $C_{\Delta\phi}$  is well consistent with the observation [Fig.3(a) in <sub>587</sub> sured Fourier amplitude  $A_l$  an offset  $\sim O(1)$ . We find 547 the main text]. The RDSs have no significant modula- 588 that the offset can effectively reduce the fitted growth 548 tion in their azimuthal density at early time  $\lesssim 20\,\mathrm{ms}$ . 589 rates. To see those systematic effects, we convolute the

550 imal value,  $C_{\Delta\phi}$  exhibits strong angular correlation at  $_{551}$   $\Delta\phi\approx 120^{\circ}$  and  $240^{\circ}$ , corresponding l=3 necklace for-552 mation. At even later time, the angular correlation at  $_{553}$   $\Delta\phi\approx180^{\circ}$  (l=2 mode) becomes comparable to the ones at  $\Delta \phi \approx 120^{\circ}$  and  $240^{\circ}$ , resulting in the competi-555 tion among those unstable modes.

In Fig. 8(c). we plot the dynamics of the Fourier They are detected using a spectrum, defined as  $A_l = \left\langle \left| \sum_{\Delta \phi} C(\phi, \Delta \phi) e^{il\Delta \phi} \right| \right\rangle_{\phi}$ . It 558 marks the rise of modulation amplitude only for lower an-559 gular frequency modes due to the finite instability band  $_{560}$   $l < l_{\rm max}$ ; l = 3 mode dominates at  $t \sim 40\,{\rm ms}$ , while  $l_{\rm max}$  approaches to  $r_{\rm min}/\xi \sim 3$  as the RDS shrinks. At  $_{562}$   $t\sim60\,\mathrm{ms},\,l=2$  and l=3 modes eventually display com-563 parable amplitudes. This dynamics naturally appears in 564 shrinking RDSs, supporting our experimental observa-565 tion of mode competition dynamics in Fig. 3 (b,c). The <sub>566</sub> detailed dynamics of  $A_l$  is plotted in Fig. 8(d). We find 567 that the amplifications in the prohibited band  $l>l_{
m max}$ 568 are incompletely terminated at  $l \geq 4$ . We attribute this 569 potentially to the contribution from adjacent RDSs (see 570 (a)) or the evolution of phonon fluctuations that may 571 not be sensitively detected in the experiment. Also, in 572 the simulation one can see a continuous reduction in  $A_l$ 573 at the early stage  $t \lesssim 20\,\mathrm{ms}$  during which the wavefunc- $_{574}$  tion expands while solitary waves develop.  $A_l$  starts to 575 grow once RDSs form.

> Figure 8(e, f) compare the experimental data  $\gamma_l$ , as 577 shown in Fig. 3(d), with the early-time growth rate  $\gamma_l^{(sim)}$ , obtained from exponential fits as in Fig. 8(d). In Fig. 8(e), the observed exponential growth within  $l \leq 6$  is 580 well reproduced by the simulation, except for an overall scaling constant  $\alpha \approx 0.17$  adjusted to match the data, in- $_{\rm 582}$  dicating that the observed rate is roughly six times lower  $_{583}$  than that in the simulation. We believe the slower rate

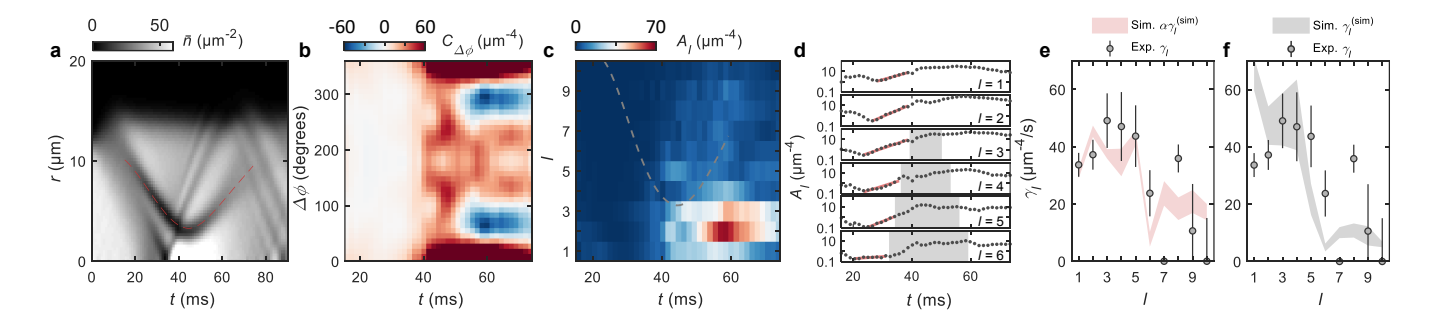


FIG. 8. Pattern-forming instability in the simulation. (a) Radial density averaged over nine runs. Dashed line represents detected radius  $\bar{r}_c$  of generated RDSs. (b) Azimuthal density-density correlation function  $C_{\Delta\phi}$ . (c) Fourier spectra  $A_l$ . Dashed line shows the maximal unstable mode  $l_{\text{max}}$ , expected from  $\bar{r}_c$  and  $\dot{\bar{r}}_c$ . (d) Dynamics of  $A_l$  in the logarithmic scale. Solid lines are exponential fits to determine the initial growth rates  $\gamma_l^{(\text{sim})}$ . Shaded area shows a regime where the mode amplification is expected to be halted  $l > l_{\text{max}}$ . (e) Experimental rates  $\gamma_l$  (dots), compared with  $\gamma_l^{(\text{sim})}$  scaled by an overall factor  $\alpha \approx 0.17$ (shaded area). Error bars and vertical width in  $\alpha \gamma_l^{(\text{sim})}$  represent fitting uncertainty. (f) Same as (e), except that  $\gamma_l^{(\text{sim})}$  is from the simulations including systematic effects. The simulated rates well reproduce the data with no free parameters.

632

643

644

<sup>591</sup> offsets to the GPE simulated amplitudes  $A_l$ . We refit <sup>594</sup> Fig. 8(f). <sub>592</sub> the growth rate  $\gamma_l^{\text{(sim)}}$  and indeed find that they agree

590 GPE data with finite resolution and add the measured 593 well with experimentally determined values as shown in

M. R. Matthews, B. P. Anderson, P. Haljan, D. Hall, C. Wieman, and E. A. Cornell, Vortices in a Bose-Einstein condensate, Phys. Rev. Lett. 83, 2498 (1999)

595

596

597

598

599

600

601

602

603

604

605

606

609

610

611

612

613

614

615

616

617

618

619

621

622

624

626

- [2] K. W. Madison, F. Chevy, W. Wohlleben, and J. Dalibard, Vortex formation in a stirred Bose-Einstein condensate, Phys. Rev. Lett. 84, 806 (2000).
- J. R. Abo-Shaeer, C. Raman, J. M. Vogels, and W. Ketterle, Observation of vortex lattices in Bose-Einstein condensates, Science 292, 476 (2001).
- W. J. Kwon, S. W. Seo, and Y.-i. Shin, Periodic shedding of vortex dipoles from a moving penetrable obstacle 640 in a Bose-Einstein condensate, Phys. Rev. A 92, 033613 641 (2015).
- [5] S. W. Seo, B. Ko, J. H. Kim, and Y.-i. Shin, Observation of vortex-antivortex pairing in decaying 2D turbulence of a superfluid gas, Scientific Reports 7, 1 (2017).
- G. Gauthier, M. T. Reeves, X. Yu, A. S. Bradley, M. A. Baker, T. A. Bell, H. Rubinsztein-Dunlop, M. J. Davis, and T. W. Neely, Giant vortex clusters in a twodimensional quantum fluid, Science **364**, 1264 (2019).
- S. P. Johnstone, A. J. Groszek, P. T. Starkey, C. J. Billington, T. P. Simula, and K. Helmerson, Evolution 651 of large-scale flow from turbulence in a two-dimensional superfluid, Science 364, 1267 (2019) .
- T. Bland, G. Lamporesi, M. J. Mark, and F. Ferlaino, 620 Vortices in dipolar Bose-Einstein condensates, arXiv preprint arXiv:2303.13263 (2023).
- W. Kwon, G. Del Pace, K. Xhani, L. Galantucci, 623 A. Muzi Falconi, M. Inguscio, F. Scazza, and G. Roati, Sound emission and annihilations in a programmable 625 quantum vortex collider, Nature 600, 64 (2021).
- [10]D. Hernández-Rajkov, N. Grani, F. Scazza, G. Del Pace, 627 W. Kwon, M. Inguscio, K. Xhani, C. Fort, M. Mod-628

- ugno, F. Marino, et al., Universality of the superfluid Kelvin-Helmholtz instability by single-vortex tracking, arXiv preprint arXiv:2303.12631 (2023).
- [11] S. Burger, K. Bongs, S. Dettmer, W. Ertmer, K. Sengstock, A. Sanpera, G. V. Shlyapnikov, and M. Lewenstein, Dark solitons in Bose-Einstein condensates, Phys. Rev. Lett. **83**, 5198 (1999).
- J. Denschlag, J. E. Simsarian, D. L. Feder, C. W. Clark, [12]L. A. Collins, J. Cubizolles, L. Deng, E. W. Hagley, K. Helmerson, W. P. Reinhardt, et al., Generating solitons by phase engineering of a Bose-Einstein condensate, Science 287, 97 (2000).
- M. J. H. Ku, B. Mukherjee, T. Yefsah, and M. W. Zwier-[13]lein, Cascade of solitonic excitations in a superfluid Fermi gas: From planar solitons to vortex rings and lines, Phys. Rev. Lett. 116, 045304 (2016).
- Z. Dutton, M. Budde, C. Slowe, and L. V. Hau, Ob-645 servation of quantum shock waves created with ultra-646 compressed slow light pulses in a Bose-Einstein condensate, Science 293, 663 (2001). 648
- N. S. Ginsberg, J. Brand, and L. V. Hau, Observation 649 of hybrid soliton vortex-ring structures in Bose-Einstein condensates, Phys. Rev. Lett. 94, 040403 (2005) .
- B. Anderson, P. Haljan, C. Regal, D. Feder, L. Collins, 652 C. W. Clark, and E. A. Cornell, Watching dark solitons 653 decay into vortex rings in a Bose-Einstein condensate, 654 655 Phys. Rev. Lett. 86, 2926 (2001).
- C. Becker, S. Stellmer, P. Soltan-Panahi, S. Dörscher, 656 M. Baumert, E.-M. Richter, J. Kronjäger, K. Bongs, and K. Sengstock, Oscillations and interactions of dark and dark-bright solitons in Bose-Einstein condensates, Nature Physics 4, 496 (2008).
  - A. Weller, J. P. Ronzheimer, C. Gross, J. Esteve, M. K. Oberthaler, D. J. Frantzeskakis, G. Theocharis, and P. G.

Kevrekidis, Experimental observation of oscillating and 727 interacting matter wave dark solitons, Phys. Rev. Lett. 728 **101**, 130401 (2008).

663

664

665

- I. Shomroni, E. Lahoud, S. Levy, and J. Steinhauer, Evi-730 666 dence for an oscillating soliton/vortex ring by density en-667 gineering of a Bose–Einstein condensate, Nature Physics 668 **5**, 193 (2009). 669
- J. J. Chang, P. Engels, and M. A. Hoefer, Forma-670 tion of dispersive shock waves by merging and splitting 671 Bose-Einstein condensates, Phys. Rev. Lett. 101, 170404 672 673
- C. N. Weiler, T. W. Neely, D. R. Scherer, A. S. Bradley, 674 M. J. Davis, and B. P. Anderson, Spontaneous vortices in 675 the formation of Bose-Einstein condensates, Nature 455, 676 677
- D. Freilich, D. Bianchi, A. Kaufman, T. Langin, and 742 678 D. Hall, Real-time dynamics of single vortex lines and 679 vortex dipoles in a Bose-Einstein condensate, Science 680 **329**, 1182 (2010). 681
- [23] G. Lamporesi, S. Donadello, S. Serafini, F. Dalfovo, and 746 682 G. Ferrari, Spontaneous creation of Kibble-Zurek soli-683 tons in a Bose-Einstein condensate, Nature Physics 9, 684 656 (2013). 685
- L. Chomaz, L. Corman, T. Bienaimé, R. Desbuquois, 750 686 [24] C. Weitenberg, S. Nascimbene, J. Beugnon, and J. Dal-687 ibard, Emergence of coherence via transverse condensa-688 tion in a uniform quasi-two-dimensional Bose gas, Nature communications 6, 1 (2015).
- [25] B. Ko, J. W. Park, and Y.-i. Shin, Kibble-Zurek univer-691 sality in a strongly interacting Fermi superfluid, Nature 692 Physics 15, 1227 (2019). 693
- [26] P. G. Kevrekidis and D. J. Frantzeskakis, Pattern form-694 ing dynamical instabilities of Bose–Einstein condensates. 695 Modern Physics Letters B 18, 173 (2004). 696
- [27]Y. S. Kivshar and D. E. Pelinovsky, Self-focusing and 761 697 transverse instabilities of solitary waves. Physics Reports 698 **331**, 117 (2000). 699
- C. Becker, K. Sengstock, P. Schmelcher, P. Kevrekidis, [28] 700 and R. Carretero-González, Inelastic collisions of solitary 765 701 waves in anisotropic Bose-Einstein condensates: sling- 766 702 shot events and expanding collision bubbles, New Journal 703 of Physics 15, 113028 (2013). 704
- S. Donadello, S. Serafini, M. Tylutki, L. P. Pitaevskii, 769 705 F. Dalfovo, G. Lamporesi, and G. Ferrari, Observation 770 706 707 of solitonic vortices in Bose-Einstein condensates, Phys. 771 Rev. Lett. **113**, 065302 (2014). 708
- Y. S. Kivshar and X. Yang, Ring dark solitons, Phys. 773 709 Rev. E **50**, R40 (1994). 710
- Y. S. Kivshar and B. Luther-Davies, Dark optical soli-711 tons: physics and applications, Physics reports 298, 81 712 713
- [32] D. Frantzeskakis, Dark solitons in atomic Bose– 714 Einsteincondensates: from theory to experiments, Jour- 779 715 nal of Physics A: Mathematical and Theoretical 43, 716 213001 (2010). 717
- L. A. Toikka and K.-A. Suominen, Snake instability of 782 [33] 718 ring dark solitons in toroidally trapped Bose-Einstein 783 719 condensates, Phys. Rev. A 87, 043601 (2013) . 720
- G. Theocharis, D. J. Frantzeskakis, P. G. Kevrekidis, 785 721 B. A. Malomed, and Y. S. Kivshar, Ring dark solitons 786 722 and vortex necklaces in Bose-Einstein condensates, Phys. 723 Rev. Lett. 90, 120403 (2003). 724
- [35] V. Pietilä, M. Möttönen, T. Isoshima, J. A. M. Huh-725 tamäki, and S. M. M. Virtanen, Stability and dynamics 790 726

- of vortex clusters in nonrotated Bose-Einstein condensates, Phys. Rev. A 74, 023603 (2006) .
- L.-C. Crasovan, G. Molina-Terriza, J. P. Torres, L. Torner, V. M. Pérez-García, and D. Mihalache, Globally linked vortex clusters in trapped wave fields, Phys. Rev. E 66, 036612 (2002).
- M. Möttönen, S. M. M. Virtanen, T. Isoshima, and M. M. Salomaa, Stationary vortex clusters in nonrotating Bose-Einstein condensates, Phys. Rev. A 71, 033626 (2005)

734

735

736

737

738

739

741

747

754

755

756

758

759

760

775

776

777

778

780

784

- M. Cawte, M. Reeves, and A. Bradley, Neutral vortex necklace in a trapped planar superfluid, Journal of Low Temperature Physics **202**, 310 (2021).
- E. Novikov, Dynamics and statistics of a system of vor-740 tices, Zh. Eksp. Teor. Fiz 68, 2 (1975).
  - [40]L. Toikka, O. Kärki, and K. Suominen, Creation and revival of ring dark solitons in an annular Bose-Einstein condensate, Journal of Physics B: Atomic, Molecular and Optical Physics 47, 021002 (2013)
  - S. Baluschev, A. Dreischuh, I. Velchev, S. Dinev, and O. Marazov, Generation and evolution of twodimensional dark spatial solitons, Phys. Rev. E 52, 5517 (1995).
  - [42]A. Dreischuh, D. Neshev, G. G. Paulus, F. Grasbon, and H. Walther, Ring dark solitary waves: Experiment versus theory, Phys. Rev. E 66, 066611 (2002).
- M. A. Hoefer, M. J. Ablowitz, I. Coddington, E. A. Cor-753 nell, P. Engels, and V. Schweikhard, Dispersive and classical shock waves in Bose-Einstein condensates and gas dynamics, Phys. Rev. A 74, 023623 (2006) .
- L. Dominici, M. Petrov, M. Matuszewski, D. Bal-757 [44] larini, M. De Giorgi, D. Colas, E. Cancellieri, B. Silva Fernández, A. Bramati, G. Gigli, et al., Realspace collapse of a polariton condensate. Nature communications **6**, 1 (2015).
- W. Wan, S. Jia, and J. W. Fleischer, Dispersive [45]762 superfluid-like shock waves in nonlinear optics, Nature Physics 3, 46 (2007).
  - N. Navon, R. P. Smith, and Z. Hadzibabic, Quantum gases in optical boxes, Nature Physics 17, 1334 (2021).
- E. J. Halperin and J. L. Bohn, Quench-produced solitons 767 [47] in a box-trapped Bose-Einstein condensate, Phys. Rev. Research 2, 043256 (2020).
  - O. Gamayun, Y. V. Bezvershenko, and V. Cheianov, Fate of a gray soliton in a quenched Bose-Einstein condensate, Phys. Rev. A **91**, 031605 (2015).
  - [49]F. Franchini, A. Gromov, M. Kulkarni, and A. Trombettoni, Universal dynamics of a soliton after an interaction quench, Journal of Physics A: Mathematical and Theoretical 48, 28FT01 (2015).
  - J. Ruostekoski, B. Kneer, W. P. Schleich, and G. Rempe, Interference of a Bose-Einstein condensate in a hard-wall trap: From the nonlinear Talbot effect to the formation of vorticity, Phys. Rev. A 63, 043613 (2001).
- [51] M. Sciacca, C. F. Barenghi, and N. G. Parker, Matter-781 wave dark solitons in boxlike traps, Phys. Rev. A 95, 013628 (2017).
  - [52]M. Ma, R. Carretero-González, P. G. Kevrekidis, D. J. Frantzeskakis, and B. A. Malomed, Controlling the transverse instability of dark solitons and nucleation of vortices by a potential barrier, Phys. Rev. A 82, 023621 (2010).
- 789 C. A. Jones and P. H. Roberts, Motions in a Bose condensate. IV. Axisymmetric solitary waves, Journal of Physics

A: Mathematical and General 15, 2599 (1982).

791

- 792 [54] C. Jones, S. Putterman, and P. Roberts, Motions in a 830
   793 Bose condensate. V. Stability of solitary wave solutions 831
   794 of non-linear Schrödinger equations in two and three dimensions, Journal of Physics A: Mathematical and General 19, 2991 (1986) .
- 797 [55] W. J. Kwon, G. Moon, J.-y. Choi, S. W. Seo, and Y.-i.
   798 Shin, Relaxation of superfluid turbulence in highly oblate
   799 Bose-Einstein condensates, Phys. Rev. A 90, 063627
   800 (2014) .
- 801 [56] N. Meyer, H. Proud, M. Perea-Ortiz, C. O'Neale,
   802 M. Baumert, M. Holynski, J. Kronjäger, G. Barontini,
   803 and K. Bongs, Observation of two-dimensional local 804 ized Jones-Roberts solitons in Bose-Einstein condensates,
   805 Phys. Rev. Lett. 119, 150403 (2017) .
- Edding
   Bose-Einstein condensate, Phys. Rev. Lett. 104, 160401 (2010)
   Bose-Einstein condensate, Phys. Rev. Lett. 104, 160401 (2010)
- 810 [58] R. Du, J.-C. Xing, B. Xiong, J.-H. Zheng, and T. Yang,
   Ruench dynamics of Bose–Einstein condensates in box 812 like traps, Chinese Physics Letters 39, 070304 (2022).
- 813 [59] Z.-X. Niu and C. Gao, Dynamical nonlinear excita 814 tions induced by interaction quench in a two-dimensional
   815 box-trapped Bose-Einstein condensate, arXiv preprint
   816 arXiv:2303.08972 (2023) .
- 817 [60] W. Wang, P. G. Kevrekidis, R. Carretero-González, D. J.
  818 Frantzeskakis, T. J. Kaper, and M. Ma, Stabilization of
  819 ring dark solitons in Bose-Einstein condensates, Phys.
  857 Rev. A 92, 033611 (2015) .
  858
- 821 [61] S. Serafini, L. Galantucci, E. Iseni, T. Bienaimé, R. N. 859 [72]
   822 Bisset, C. F. Barenghi, F. Dalfovo, G. Lamporesi, and 860
   823 G. Ferrari, Vortex reconnections and rebounds in trapped 861
   824 atomic Bose-Einstein condensates, Physical Review X 7, 862
   825 021031 (2017) . 863 [73]
- 826 [62] T. Simula, M. J. Davis, and K. Helmerson, Emergence 864
   827 of order from turbulence in an isolated planar superfluid, 865
   828 Phys. Rev. Lett. 113, 165302 (2014) .

- [63] T. P. Billam, M. T. Reeves, B. P. Anderson, and A. S. Bradley, Onsager-kraichnan condensation in decaying two-dimensional quantum turbulence, Phys. Rev. Lett. 112, 145301 (2014).
- E33 [64] T. Kanai and W. Guo, True mechanism of spontaneous order from turbulence in two-dimensional superfluid manifolds, Phys. Rev. Lett. 127, 095301 (2021) .
- 836 [65] C.-A. Chen and C.-L. Hung, Observation of universal
   837 quench dynamics and Townes soliton formation from
   838 modulational instability in two-dimensional Bose gases,
   839 Phys. Rev. Lett. 125, 250401 (2020) .
- 840 [66] C. Chin, R. Grimm, P. Julienne, and E. Tiesinga, Fesh841 bach resonances in ultracold gases, Rev. Mod. Phys. 82,
  842 1225 (2010) .
- <sup>843</sup> [67] C.-L. Hung, In situ probing of two-dimensional quantum
   gases (The University of Chicago, 2011) .
- 845 [68] K. E. Wilson, Z. L. Newman, J. D. Lowney, and B. P.
   846 Anderson, In situ imaging of vortices in Bose-Einstein
   847 condensates, Phys. Rev. A 91, 023621 (2015) .
- 848 [69] R. J. Fletcher, A. Shaffer, C. C. Wilson, P. B. Patel,
   849 Z. Yan, V. Crépel, B. Mukherjee, and M. W. Zwierlein,
   850 Geometric squeezing into the lowest landau level, Science
   851 372, 1318 (2021) .
- R52 [70] V. A. Brazhnyi, V. V. Konotop, and L. P. Pitaevskii,
   Dark solitons as quasiparticles in trapped condensates,
   Phys. Rev. A 73, 053601 (2006) .
  - [71] X. Antoine and R. Duboscq, GPELab, a Matlab toolbox to solve Gross-Pitaevskii equations I: Computation of stationary solutions, Computer Physics Communications 185, 2969 (2014).
  - [72] X. Antoine and R. Duboscq, GPELab, a Matlab tool-box to solve Gross-Pitaevskii equations II: Dynamics and stochastic simulations, Computer Physics Communications 193, 95 (2015).
- Rakonjac, A. L. Marchant, T. P. Billam, J. L. Helm,
   M. M. H. Yu, S. A. Gardiner, and S. L. Cornish, Measuring the disorder of vortex lattices in a Bose-Einstein condensate, Phys. Rev. A 93, 013607 (2016) .